Holocene sea ice and paleoenvironment conditions in the Beaufort Sea (Canadian Arctic) reconstructed with lipid biomarkers

Madeleine Santos[1,2], Lisa Bröder[1], Matt O'Regan[3,4], Iván Hernández-Almeida[1,5], Tommaso Tesi[6], Lukas Bigler[1,7], Negar Haghipour[1,8], Daniel B. Nelson[2], Michael Fritz[9], Julie Lattaud[1,2,7]

[1]Department of Earth and Planetary Sciences, ETHZ, Zurich, 8092 Switzerland

[2]Department of Environmental Science, University of Basel, Basel, 4056, Switzerland

[3]Department of Geological Sciences, Stockholm University, Stockholm, 106 91, Sweden

[4]Bolin Centre for Climate Research, – Stockholm University, Stockholm, 106 91, Sweden

[5]Past Global Changes, University of Bern, Bern, 3012, Switzerland

[6]Institute of Polar Sciences (ISP), Bologna, 40129, Bologna 40128, Italy

[7]Department of Environmental Science, Stockholm University, Stockholm, 106 91, Sweden

[8]Laboratory of Ion Beam Physics, ETHZ, Zurich, 8092, Switzerland

[9]Alfred Wegener Institute, Helmholtz Centre for Polar and Marine Research, Potsdam, 14473, Germany

Correspondence to: Julie Lattaud (Julie.lattaud@aces.su.se)

Abstract The Beaufort Sea region in the Canadian Arctic has undergone substantial sea ice loss in recent decades, primarily driven by anthropogenic climate warming. To place these changes within the context of natural climate variability, Holocene sea ice evolution and environmental conditions (sea surface temperature, salinity, terrestrial input) were reconstructed using lipid biomarkers (HBIs including IP_{25}, OH-GDGT, brGDGT, $C_{16:0}$ fatty acid, phytosterols) from two marine sediment cores collected from the Beaufort Shelf and slope, spanning the past 9.1 ka and 13.3 cal. kyr BP, respectively. The Early Holocene (11.7-8.2 ka) is characterized by relatively higher sea surface temperature, lower salinity and no spring/summer sea ice until 8.5 ka on the Beaufort Sea slope. Around 8.5 ka, a peak in organic matter content is linked to both increased terrestrial input and primary production and may indicate increased riverine input from the Mackenzie River and terrestrial matter input from coastal erosion. Following this period, terrestrial inputs decreased throughout the Mid-Holocene in both cores. A gradual increase in IP_{25} and HBI-II concentrations aligns with relatively higher salinity, lower sea surface temperature and rising sea levels, and indicate the establishment of seasonal (spring) sea ice on the outer shelf around 7 ka and on the shelf around 5 ka. These patterns suggest an expansion of the sea ice cover beginning in the Mid-Holocene, influenced by decreasing summer insolation. During the Late Holocene (4.2–1 ka), permanent sea ice conditions are inferred on the slope with a peak during the Little Ice Age. After 1 ka, seasonal sea ice conditions on the slope are observed again, alongside an increase in salinity and terrestrial input, and variable primary productivity. Similar patterns of Holocene sea ice variability have been observed across other Arctic marginal seas, highlighting a consistent response to external climate forcing. Continued warming may drive the Beaufort Sea toward predominantly ice-free conditions, resembling those inferred for the Early Holocene.

1. Introduction

Sea ice is a critical component of the Arctic climate system, influencing ocean–atmosphere interactions, modulating surface albedo (Kashiwase et al., 2017), regulating heat fluxes (Lake, 1967), and influencing ecosystem structure through its control on light penetration and nutrient cycling (Lannuzel et al., 2020). Its high sensitivity to temperature makes it both a driver and indicator of Arctic climate change. Since the late 1970s, satellite observations have revealed a significant decline in Arctic sea ice extent, sparking interest in the mechanisms that govern sea ice variability over multiple timescales (Stroeve et al., 2012). The Canadian Beaufort Sea is a marginal sea of the western Arctic Ocean which exhibits strong seasonal and interannual variability in sea ice cover. Characterized by landfast ice on the shelf and mobile pack ice offshore, this region has experienced significant sea-ice loss in recent decades due to rising atmospheric and oceanic temperatures (Carmack et al., 2015; Comiso et al., 2008).

Understanding natural variability of sea-ice prior to the industrial era is critical for contextualizing recent trends. Throughout the Holocene, Arctic sea ice has responded to changes in orbital forcing, ocean circulation, and ice sheet dynamics (Park et al., 2018; Stein et al., 2017). During the Late glacial, abrupt climatic events such as Bølling-Allerød (~14 – 12.8 ka) and Younger Dryas (~12.8–11.7 ka), contributed to the instability of the Arctic cryosphere. In the Canadian Arctic, enhanced meltwater discharge and re-routing following the retreat of the Laurentide Ice Sheet (LIS) contributed to oceanographic shifts and transient cooling events (Broecker et al., 1989). Lipid biomarker records and climate simulations from the Arctic suggest reduced sea ice during the Early Holocene thermal maximum (11–6 ka in the Canadian Arctic) (Kaufman et al., 2004), followed by expansion through the Middle to Late Holocene, consistent with declining summer insolation (Stranne et al., 2014; Wu et al., 2020). Numerous studies on Arctic sea ice variability have focused on offshore locations highlighting heterogeneity in sea-ice cover history and the importance of local currents (Belt et al., 2010; Detlef et al., 2023; Fahl & Stein, 2012; Hörner et al., 2016, 2018; Stein et al., 2017; Stein & Fahl, 2012; Vare et al., 2009; J. Wu et al., 2020). However, these studies often neglected the spatial extent of sea ice cover toward the coast and the migration of the marginal ice zone.

Sea-ice cover can be reconstructed from microfossil and lipid biomarker evidence preserved in marine sediments. Remains of sea-ice organisms such as dinocysts (de Vernal et al., 2013) and diatoms, the latter producing a specific biomarker known as IP_{25} (Belt et al., 2007), provide valuable records of past sea-ice conditions. This highly branched isoprenoid (HBI) and its isomer HBI diene (HBI-II) are used to trace the presence of spring sea-ice in

64   modern and geological settings (e.g., Belt et al., 2010; Fahl & Stein, 2012; Hörner et al., 2016, 2018; Vare et al.,

65   2009). However, because the absence of these two HBIs may reflect either a permanent sea-ice condition (due to the

66   absence of light) or completely sea-ice free waters, the PIP_{25} ratio was developed (Müller et al., 2011). This ratio

67   includes a phytoplankton biomarker (typically dinosterol, brassicasterol or HBI-III) that represents open-water

68   productivity. PIP_{25} values have been used to distinguish between seasonal sea-ice (>0.5) and permanent sea-ice

69   cover (>0.75).

70   Sea-ice cover is influenced by both the atmospheric and the oceanic forcing, including salinity and temperature,

71   parameters that are often difficult to reconstruct in polar regions. Lipid biomarker and their (isotopic) ratios are a

72   useful toolkit for this purpose. In particular, compound-specific hydrogen isotopes of phytoplankton biomarkers

73   have shown promise for reconstructing past salinity (e.g., Lattaud et al., 2019; Sachs et al., 2018; Weiss et al., 2019).

74   However, in the Arctic Ocean, the generally low abundances of lipid biomarker restrict this approach to the

75   dominant lipid biomarkers, such as palmitic acid ($C_{16:0}$ fatty acid, Sachs et al., 2018). In contrast to salinity, several

76   established proxies exist for reconstructing seawater temperature, including microfossil assemblages (e.g., dinocyst,

77   Richerol et al., 2008), inorganic ratios (e.g., Mg/Ca of foraminifera, Barrientos et al., 2018; Kristjánsdóttir et al.,

78   2007) and lipid biomarkers (Ruan et al., 2017; Varma et al., 2024). Among lipid biomarker proxies for cold water (<

79   15°C) environments, hydroxylated glycerol dialkyl glycerol tetraether (OH-GDGT) are particularly useful, with RI-

80   OH' and TEX-OH identified as promising seawater temperature indices (Lü et al., 2015; Varma et al., 2024).

81   Nevertheless, even the latest calibrations (Varma et al., 2024) reveal substantial uncertainty at low temperatures,

82   partly due to the limited representation of polar core-top sediments, which are biased toward the European and

83   Russian Arctic. These limitations highlight the need to further develop and test Arctic-specific proxies for both

84   salinity and seawater temperature.

85   This study presents a multi-proxy reconstruction of Holocene sea ice and oceanographic variability from two

86   sediment cores (PCB09, PCB11) collected from the Beaufort outer shelf and shelf slope. Lipid biomarkers,

87   including highly branched isoprenoids (HBIs), glycerol dialkyl glycerol tetraethers (GDGTs), the hydrogen isotopic

88   compositions of algal-derived fatty acids and terrestrial sterols, are used to reconstruct sea-ice cover, sea surface

89   temperatures (SSTs), salinity and terrestrial organic matter input. Additionally, a set of surface sediments is used to

90   assess the applicability and calibrate salinity and SST proxies in sediments of the Beaufort Sea.

91 The primary objectives are to (1) reconstruct past variations in sea-ice cover on the Beaufort Shelf throughout the

92 Holocene, (2) explore the potential roles of insolation changes, meltwater input, and oceanic conditions in shaping

93 regional sea-ice variability, and (3) place the Beaufort Sea record within a broader Arctic context to provide insights

94 into past and present climate variability.

95 **2. Materials and Methods**

96 **2.1. Study area**

97 The study focuses on the Canadian Beaufort Sea, one of the marginal seas of the Arctic Ocean (Fig. 1), bounded by

98 the glacially excavated Amundsen Gulf to the east, Mackenzie Trough to the west, and the Mackenzie River delta to

99 the south (Carmack et al., 2004). The shelf is a large estuarine setting at the interface between the Arctic Ocean and

100 the Mackenzie River (Omstedt et al., 1994) (Fig.1). The Mackenzie River is a significant source of freshwater to the

101 Beaufort Sea, with an annual water discharge of $316\,km^3\,yr^{-1}$ (Holmes et al., 2012) and is considered the largest

102 Arctic river in terms of sediment flux ($124–128\,Mt·yr^{-1}$) (Stein et al., 2004). At the same time, permafrost coastal

103 erosion adds another $8-9\,Mt·yr^{-1}$ of sediment into the Beaufort Sea, including carbon and nutrients (Wegner et al.,

104 2015). Surface water circulation in the Beaufort Sea is primarily characterized by the clockwise Beaufort Gyre,

105 which drives offshore currents towards the west and traps the majority of the Arctic Ocean's freshwater in the

106 Canada Basin (Serreze et al., 2006). There is also a eastward flowing shelf-break current at depths beneath $50\,m$,

107 which transports Pacific Water (coming from the Bering Strait) along the slope (Pickart, 2004). Sea ice cover on the

108 Beaufort Shelf north of the Mackenzie River Delta varies from year to year, but generally begins to form in mid-

109 October, persisting until ice break up in April-May (Fig. S1). During ice break up, an open water flaw lead occurs

110 along the outer edge of the landfast ice establishing a spring marginal ice zone over the shelf.

111 **2.2. Material**

112 Two sediment cores were analyzed in the study. They were recovered as part of the Permafrost Carbon on the

113 Beaufort Shelf (*PeCaBeau*) project during the 4th Leg of the 2021 CCGS Amundsen expedition (Bröder et al., 2022,

114 Fig.1). At station PCB09 (71.1°N, 135.1°W) at a water depth of $675\,m$ on the Beaufort shelf slope, a piston core

115 (PC, length of $420\,cm$) and multicore (MC, $30\,cm$) were retrieved (Fig. 1). At station PCB11 (70.6°N, 136.0°W) on

116 the outer Beaufort shelf ($74\,m$ water depth) a giant gravity core (GGC, length of $290\,cm$) and MC ($32\,cm$) were

117 recovered (Fig. 1). PCB09 is found within the modern Atlantic bottom water mass, while PCB11 lies within the

118 Pacific summer water (Fig. S2), the water masses were defined as in Matsuoka et al. (2012). The core tops (0-1cm)

119 from 22 multicores collected during *PeCaBeau*, were used to ground truth the hydrogen isotope ratio of $C_{16:0}$ fatty

120 acid proxy for reconstructing salinity and test the applicability of the SST reconstructions (Fig. S1).
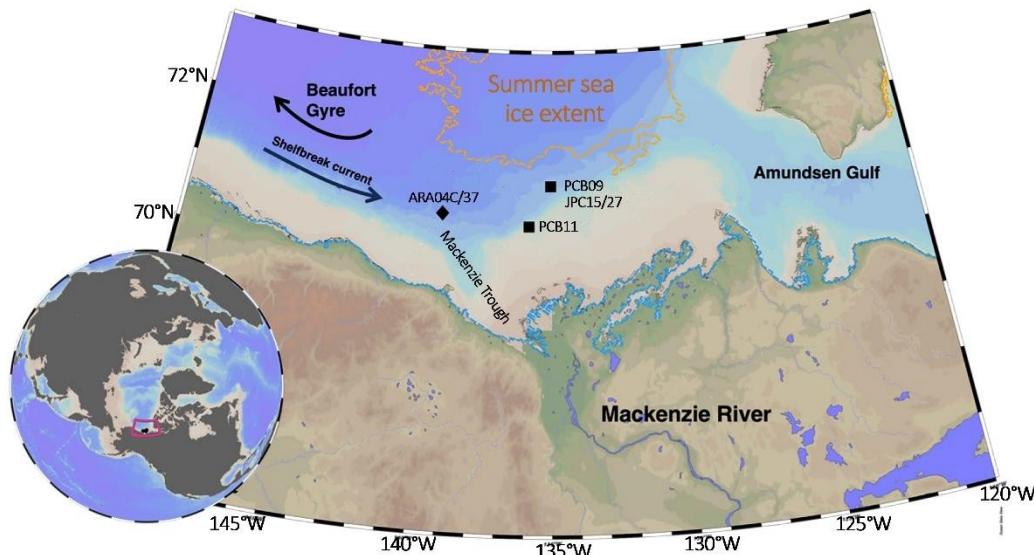
121

122 Figure 1: Combined topographic and bathymetric map of the Beaufort Shelf region (Canadian Arctic) displaying the
123 cores from this study as black squares (PCB09 and PCB11) and key records discussed in the text (ARA04C/37 from
124 Wu et al., 2020; JPC15/27 from Keigwin et al., 2018). The 2021 summer sea-ice extent is outlined by the orange
125 dotted line, the winter sea ice extent follows the coastline (Meier et al., 2018). Map generated using Ocean Data View
126 (Schlitzer, 2025).

127 **2.3. Methods**

128 **2.3.1. Core processing**

129 During the PeCaBeau expedition, all cores were scanned shipboard on a Geotek multi-sensor core logger (MSCL).

130 Bulk density and magnetic susceptibility were measured at a 1 cm downcore resolution on the piston and gravity cores,

131 (Bröder et al., 2022). The cores remained unopened and were shipped to AWI Potsdam following the expedition. They

132 were subsequently split in the fall/winter and the working halves sampled using 2x2 cm u-channels, before being cut

133 into 1-2 cm thick slices which were frozen and freeze dried.

134 An ITRAX XRF-core scanner was used to measure relative elemental abundances at Stockholm University, Sweden.

135 Measurements were performed on u-channel samples at a downcore resolution of 2 mm. Analyses were made using a

136 Mo tube at a voltage of 55 kV, a current of 50 mA and an exposure time of 20 s. Here we present the ratios of Ca/Ti,

137 reflecting detrital carbon inputs regionally elevated by meltwater delivery from either the Mackenzie or Amundsen

138 Gulf during deglaciation (Klotsko et al., 2019; Swärd et al., 2022; J. Wu et al., 2020). Zr/Rb was used as a proxy for

139 grain size variations as Zr content is elevated in coarse minerals, while Rb is associated with clay minerals (L. Wu et

140 al., 2020) and Br/Cl as a proxy for marine organic matter as Br usually correlates well with OC content (Wang et al.,

141 2019).

142 **2.3.2. Age model**

143 The chronology of the piston and gravity cores (Fig. 2) were determined by ^{14}C dating of foraminifera (n = 13,

144 PCB09) and bivalve shells (n = 7, PCB11) (Table S1). The MSCL data was used to stratigraphically correlate

145 PCB09 with JPC15/27 (Keigwin et al., 2018) allowing us to integrate existing radiocarbon ages (n=8) from this

146 record with our new data (n=5) (Fig. S3).

147 Bivalve shells were either picked from the split cores when sampling, or later from the freeze-dried sediments.

148 Foraminifera were picked from the >45 μm fraction of the wet-sieved samples following organic extractions.

149 Foraminifera samples consisted of either planktonic (*Neogloboquadrina pachyderma*), benthic, or a combination of

150 both in horizons when specimens were extremely rare. Care was given to pick well preserved foraminifera to avoid

151 age bias (Wollenburg et al., 2023). Foraminifera and mollusk samples were prepared for Accelerator Mass

152 Spectrometry (AMS) analyses at the Laboratory for Ion Beam Physics at ETHZ using procedures described in

153 (Missiaen et al., 2020) which include sieving and acid cleaning to remove impurities from the shells.

154 Radiocarbon-based age models were generated using the BACON package in R (Blaauw & Christen, 2011) and the

155 Marine20 calibration curve (Heaton et al., 2020). A reservoir age of 330 ± 41 years was applied to the Holocene-age

156 mollusc samples in PCB11 as determined by West et al. (2022) for Pacific waters entering the Arctic Ocean in the

157 Chukchi Sea. For PCB09 we applied the approach used for JPC15/27 (Keigwin et al., 2018) and for ARA04C/37 (J.

158 Wu et al., 2020) but updated for Marine20 as described by Lin et al. (2025). A reservoir correction of -150 ± 100

159 years was applied to Holocene planktic foraminifera, and a larger reservoir correction (50 ± 100 years) for the

160 bottom 4 samples (Table S1) that fall within the Younger Dryas. In our age model we also incorporate samples of

161 benthic foraminifera that were calibrated using a reservoir correction of 206 ± 67 years, determined by (West et al.,

162   2022) for Atlantic waters near the Chukchi Sea. Samples containing mixed planktic and benthic foraminifera were

163   calibrated using an average of these values (28 ± 85 years).

2.3.3. Bulk organic matter

165   For the determination of total organic carbon (TOC) content and stable carbon isotope composition ($\delta^{13}C$) at the

166   University of Basel, about 12 mg of freeze-dried sediment was weighed into each silver capsule and 1-2 drops of

167   distilled water were added. The samples were exposed to fuming hydrochloric acid (HCl, 37%) in a desiccator for

168   24 hours to remove inorganic carbon. Samples were dried (48 h, 50 °C) and analyzed using an elemental analyser

169   coupled to an isotope mass spectrometer (Sercon, Integra 2). The standards used to calculate TOC was

170   Ethylenediaminetetraacetic acid (EDTA, Sigma Aldrich) and for $\delta^{13}C$ were USGS40 (-26.389±0.042‰, IAEA),

171   USGS64 (-40.81±0.04, IAEA), and USGS65 (-20.29±0.04, IAEA). The analytical precision, defined as the standard

172   deviation of the measurement of the USGS standards for the $\delta^{13}C$ sequence was ±0.03‰.

2.3.4. Lipid biomarkers

174   Lipid biomarkers were analysed from 42 samples (every 10 cm for the first 143 cm, then every 20 cm) for PCB09

175   and 21 for PCB11 (every 20 cm). Core top samples from the MC's were also analysed for lipid biomarkers. For each

176   sample, 5 g of homogenized freeze-dried sediment was extracted using an Energy Dispersive Guided Extraction

177   (EDGE) following (Lattaud, Bröder, et al., 2021). Briefly, after extraction with dichloromethane (DCM): methanol

178   (MeOH) (9:1, v/v), the total lipid extracts (TLE) were saponified at 70 °C for two hours (with KOH in MeOH at

179   0.5M). The neutral phase was collected by liquid-liquid extraction with 10 mL of hexane, three times. The leftover

180   TLE was acidified to pH 2 and the acid phase was recovered by liquid-liquid extraction adding 10 mL hexane:DCM

181   (4:1, v/v), three times. The acid compounds were methylated by adding MeOH:HCl (95:5, v/v) and heated at 70°C

182   overnight. The methylated fatty acids were recovered by liquid-liquid extraction (three times) with 10 mL

183   hexane:DCM (4:1, v/v). Internal standards were added to the neutral fraction prior to silica chromatography: 7-

184   hexylnonadecane (7-HND, provided by S. Belt), 9-octylheptadec-8-ene (9-OHD, provided by S. Belt), C_{22} 5,16-diol

185   (Interbioscreen), $C_{36:0}$ alkane (Sigma Aldrich) and C_{46} GDGT-like compound(C_{46} glycerol trialkyl glycerol

186   tetraether, GTGT, Huguet et al., 2006). The neutral phase was separated into three fractions (F1, F2, and F3) through

187   silica column (combusted and deactivated 1%) using hexane:DCM (9:1, v/v), DCM, and DCM: MeOH (1:1, v/v),

188   respectively.

189   The F1 containing HBIs was analyzed on a GC-MS (Agilent 7890-5977A) operating in Selective Ion Monitoring

190   (SIM) mode at the Institute of Polar Sciences (ISP), Bologna, Italy, following (Belt et al., 2014). The column used

191   was a J&W DB5-MS (length 30 m, id 250 μm, 0.25 μm thickness). Integrations were done in SIM mode for IP_{25}

192   (m/z = 350), HBI II (m/z = 348) and HBI III and HBI IV (m/z = 346). Concentrations of IP_{25} were corrected for m/z

193   348 influence (4 %) and instrumental response factor. 9-OHD (m/z 350) was used to quantify HBIs. A reference

194   sediment containing known amount of IP_{25} was run in parallel to correct IP_{25} concentration.

195   F3 was split in two with one aliquot that was filtered using a polytetrafluoroethylene filter (PTFE, 0.45 μm pore

196   size) and analyzed for GDGTs with high performance liquid chromatography (LC)/atmospheric pressure chemical

197   ionization–MS on an Agilent 1260 Infinity series LC-MS according to Hopmans et al. (2016) with the adaptation of

198   Lattaud, De Jonge, et al. (2021). GDGTs were quantified using the C_{46} GTGT internal standard assuming the same

199   response factor.

200   The other F3 aliquot was silylated with bis(trimethylsilyl)trifluoroacetamid (BSTFA) (70 °C 30 min) and analysed at

201   the ISP for sterol concentration (brassicasterol, stigmasterol, β-sitosterol, campesterol) on a GC-MS. The C_{22} 5,16-

202   diol is used to quantify sterols. Specific m/z ratios have been extracted from chromatograms in order to identify each

203   biomarker according to their respective mass spectra, sterols were quantified on the total ion current.

204   Lipid δ^2H values were analyzed by GC coupled to an isotope ratio mass spectrometer (IRMS) on all acid fractions

205   having adequate compound abundance. Samples were analyzed using splitless injection with a split/splitless inlet at

206   280 °C and a Restek Rtx-5MS GC column (30 m × 0.25 mm × 0.25 μm) with helium carrier gas at 1.4 mL min^{-1}. The

207   GC oven was held at 60°C for 1.5 min, ramped to 140°C at 15°C min^{-1}, then to 325 °C at 4 °C min^{-1}, and held for

208   15 min. Column effluent was pyrolyzed at 1420°C, and δ^2H values were measured on a Thermo Delta V Plus IRMS.

209   The H_3^+ factor was evaluated with each measurement sequence to confirm stability. Values were always lower than

210   3 ppm mV^{-1}. Reference standards with known isotopic compositions (Mix A7, USGS71, $C_{30:0}$ FAME; provided by

211   Arndt Schimmelmann, Indiana University, USA) were analyzed alongside samples to normalize values to the

212   Vienna Standard Mean Ocean Water- Standard Light Antarctic Precipitation (VSMOW-SLAP) scale. Standards

213   were injected at a range of concentrations so that peak size effects could be assessed and corrected for. Quality

214   control samples with known δ^2H values were measured as unknowns to check precision and accuracy ($C_{16:0}$ FAME

215 in mix F8-40, $C_{30:0}$ FAME; Arndt Shimmelmann), which were 4.2 ‰ or better, and 1.0 ‰ or better, respectively (n =

216 13-16). Final fatty acid δ^2H values of $C_{16:0}$ were corrected for added hydrogen during methylation following [Eq. 1].

217 $$\delta^2H_{C16:0} = \frac{(nH_{FAME}+nH_{CH3}) \times \delta^2H_{FAME}measured - nH_{CH3} \times \delta^2H_{CH3}}{nH_{FAME}}$$ (1)

218 Where $nH_{CH3} = 3$, $nH_{FAME} = 32$.

2.3.5. Biomarker ratios and environmental indicator reconstructions (sea ice, salinity, SSTs)

220 In order to describe sea ice variability in the Holocene, the PIP_{25} index is used (Müller et al., 2011). The PIP_{25} index

221 [Eq. 2] uses additional phytoplankton biomarkers (i.e. brassicasterol, dinosterol, and HBI-III) which indicate open

222 water conditions to compare with the abundance of IP_{25} (Belt et al., 2007):

223 $$PIP_{25} = \frac{IP_{25}}{[IP_{25}]+[Phytoplankton\ biomarker]*c}$$ (2)

224 HBI-III was used in this study (Belt et al., 2015; Kolling et al., 2020; Köseoğlu et al., 2018; Smik et al., 2016) as a

225 reference for pelagic phytoplankton to derive $P_{III}IP_{25}$ index (afterward called PIP_{25}). Dinosterol was not detected in

226 the samples which is common in the Beaufort Sea (Fu et al., 2025), and brassicasterol has been shown to derive mainly

227 from terrestrial input in the region (J. Wu et al., 2020). The c value represents the ratio of the mean concentration of

228 IP_{25} over the mean concentration of HBI-III of all samples for each core (4.79 for PCB09 and 5.55 for PCB11).

229 Surface salinity was reconstructed using the calibration between δ^2H of $C_{16:0}$ fatty acid (palmitic acid) and salinity

230 from the test study of Sachs et al. (2018) [Eq. 3], adding data from Allan et al. (2023) and after testing surface

231 sediments from multicores from the region (Fig. S4):

232 $$\delta^2H_{PA} = 4.22\ (\pm0.6)*S - 338(\pm15)$$ (3)

233 where S is salinity in practical salinity units (PSU). Based on the known calibration errors (4‰ for the δ^2H

234 measurement), reconstructed salinity should have an associated error of ± 7 PSU.

235 To reconstruct SST, hydroxylated GDGTs (OH-GDGTs) were used as the hydroxyl group in these GDGTs is

236 suggested to be an adaptation feature to regulate permeability in cold waters (Liu et al., 2012). In this study, the RI-

237 OH' [Eq. 4] and TEX-OH [Eq. 5] indexes were calculated:

238 $$\text{RI-OH'} = \frac{[\text{OH-GDGT-1}] + 2*[\text{OH-GDGT-2}]}{[\text{OH-GDGT-0}] + [\text{OH-GDGT-1}] + [\text{OH-GDGT-2}]} \qquad (4)$$

239 $$\text{TEX} - \text{OH} = \frac{\text{GDGT} - 2 + \text{GDGT} - 3 + \text{Cren isomer}}{\text{GDGT} - 2 + \text{GDGT} - 3 + \text{Cren isomer} + \text{OH} - \text{GDGT} - 0 + \text{GDGT} - 1} \qquad (5)$$

240 For the conversion from RI-OH' and TEX-OH to SST, the recent calibration of Varma et al. (2024) is used [Eq. 6 and

241 7]:

242 $$\text{RI-OH'} = 0.04 \times \text{SST} + 0.003 \qquad (6)$$

243 $$\text{TEX} - \text{OH} = 0.021 \times \text{SST} + 0.08 \qquad (7)$$

244 Several organic proxies have been used to interpret terrestrial organic matter input such as branched glycerol dialkyl

245 glycerol tetraether (brGDGTs), long chain n-alkanes, and plant sterols. BrGDGTs are membrane lipids synthesized

246 by bacteria and are known to be ubiquitous in terrestrial environments (Schouten et al., 2013). The BIT index

247 (Hopmans et al., 2004) [Eq.8] is a common indicator of terrestrial input into the marine realm:

248 $$BIT = \frac{[BrGDGT - Ia + IIa + IIIa]}{[BrGDGT - Ia + IIa + IIIa] + Crenarcheol} \qquad (8)$$

249 In addition, in situ marine production of brGDGT can occur in coastal sediments between 50 and 300 m water depth

250 (Peterse et al., 2009; Sinninghe Damsté, 2016). To assess the potential for brGDGT to be produced in situ we

251 calculated the number of cyclopentane rings present in the tetraether brGDGT ($\#\text{ring}_{tetra}$) [Eq 9]:

252 $$\#ring_{tetra} = \frac{(Ib + 2 \times Ic)}{(Ia + Ib + Ic)} \qquad (9)$$

253 **2.3.6. Micropaleontology**

254 Extracted sediments were wet sieved using a 45 µm mesh. The >45 µm fraction was dried in the oven (40 °C) and

255 picked for foraminifera using a stereoscopic microscope. Planktonic foraminifera species are identified

256 (https://www.mikrotax.org/pforams/) using the morphological descriptions compiled in Microtax and counted for each

257 sample.

258 **3. Results**

259
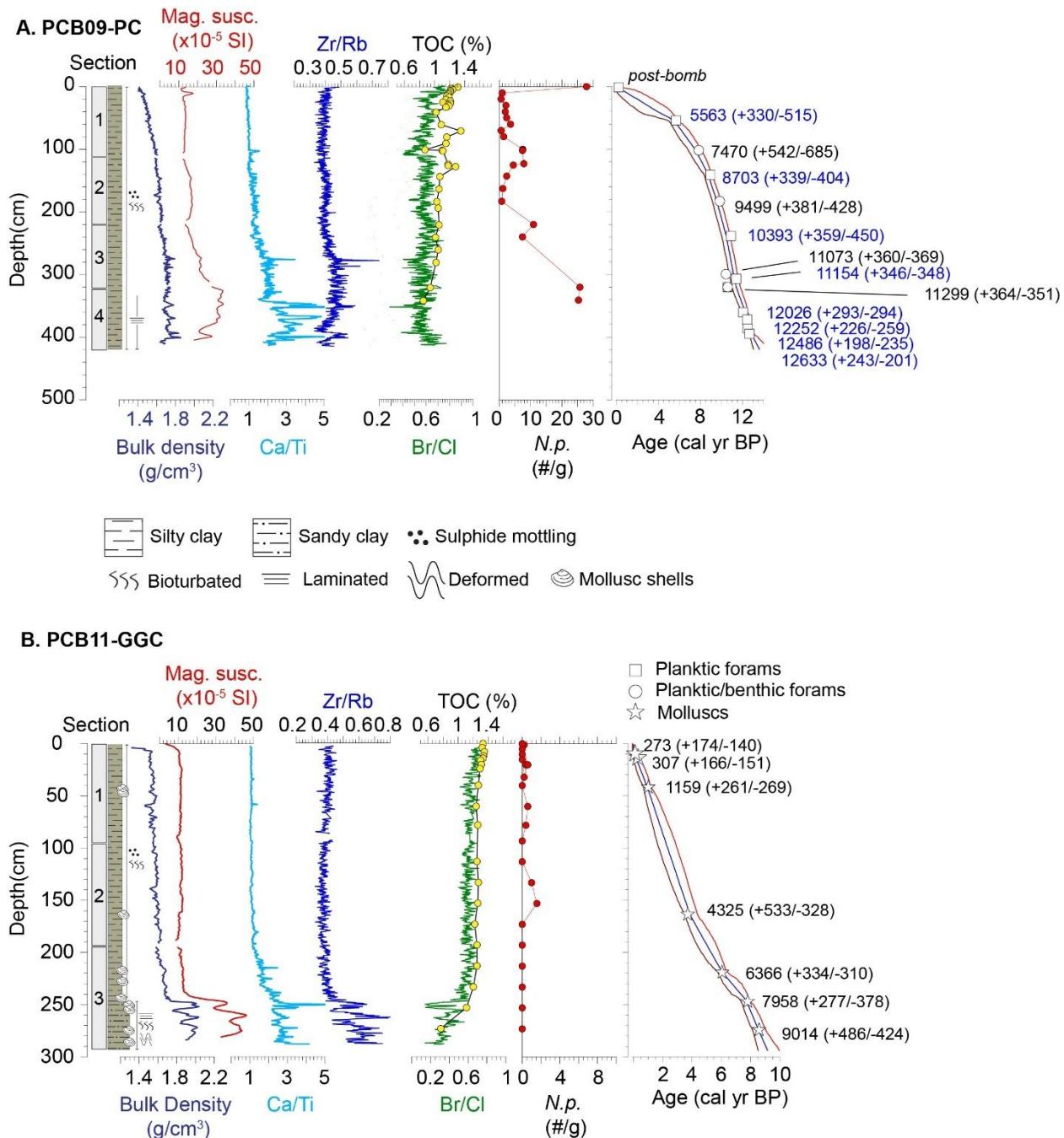
260 *Figure 2:* Core description for (a) PCB09 and (b) PCB11 presenting lithostratigraphy, bulk density, magnetic
261 susceptibility, X-Ray Fluorescence (XRF) results including Ca/Ti, Zr/Rb and Br/Cl ratios. Total organic carbon
262 content (%) and abundance of *N. pachyderma* (*N. p.*, number/gram of sediment) as well as the age models of PCB09
263 and PCB11 generated using the Bacon Rpackage (Blaauw & Christen, 2011). The red bands illustrate the 95%
264 confidence level around the modelled median age (blue line). Symbols indicate the calibrated age of the dated material
265 before age-modelling. The errors on these are lower than the symbol size. The numbers are the median modelled ages

266 and 95% error at the location of each sample. Blue radiocarbon ages originated from nearby core HLY13-15JPC
267 (Keigwin et al., 2018).

3.1. Core chronology, lithostratigraphy and bulk organic matter

269 The age models of cores PCB09 (Fig. 2a) and PCB11 (Fig. 2b) show that they cover the last 13350 ± 690 cal. yr BP

270 and 9120 ± 720 cal. yr BP, respectively. PCB11 had a mean sedimentation rate of 35 ± 10 cm kyr^{-1} with slightly

271 higher sedimentation rates in the Late Holocene (< 4 ka). Conversely, PCB09 had an average sedimentation rate of

272 $50 +/-27$ cm kyr^{-1}, with substantially higher sedimentation rates before the Late Holocene.

273 The upper 300 cm of PCB09 (0 – 11 ka) display a gradual downcore increase in bulk density, reflecting porosity loss

274 in largely homogenous silty-clay sediments (Fig 2a). Below 300 cm, slightly higher variability in the bulk density,

275 elevated magnetic susceptibility and higher Zr/Rb all point towards a transition to slightly coarser-grained sediments.

276 Ca/Ti tended to increase downcore becoming more variable below 105 cm (7.6 ± 0.6 cal yr BP). There was a notable

277 stepwise increase in Ca/Ti at 345 cm (11.7 ± 0.4 ka, Fig. 2a). Discrete peaks in Zr/Rb and bulk density, indicative of

278 sediment coarsening, co-occurred with elevated Ca/Ti ratios at depths of 276 cm (10.8 ± 0.4 cal. yr BP), 345-352 cm

279 (11.8 ± 0.4 cal. yr BP) and 402 cm (12.8 ± 0.4 cal. yr BP).

280 A similar pattern is seen in PCB11, where below 240 cm (7.4 ± 0.6 cal yr BP) there was an abrupt increase in bulk

281 density, magnetic susceptibility, Zr/Rb and Ca/Ti. TOC concentrations and the Br/Cl ratio (which mirrors small scale

282 changes in the TOC) also decreased notably through this interval (Fig. 2b, 3a). This lithologic transition post-dates

283 the Late glacial and Early Holocene detrital carbonate inputs in cores recovered from the Beaufort Sea slope (Klotsko

284 et al., 2019). It is likely that this coarser basal facies is related to the inundation of the shelf during transgression.

285 Bulk sediment $\delta^{13}C$ of PCB09 was lowest in the Early Holocene at approximately -26.3‰ until 8.7 ± 0.4 ka, before

286 increasing during the Middle and Late Holocene to -24.7‰ (Fig. 3b). The trend in $\delta^{13}C$ in PCB11 is similar to

287 PCB09 showing a steady increase over time from -26.5‰ to -25.8‰.

288
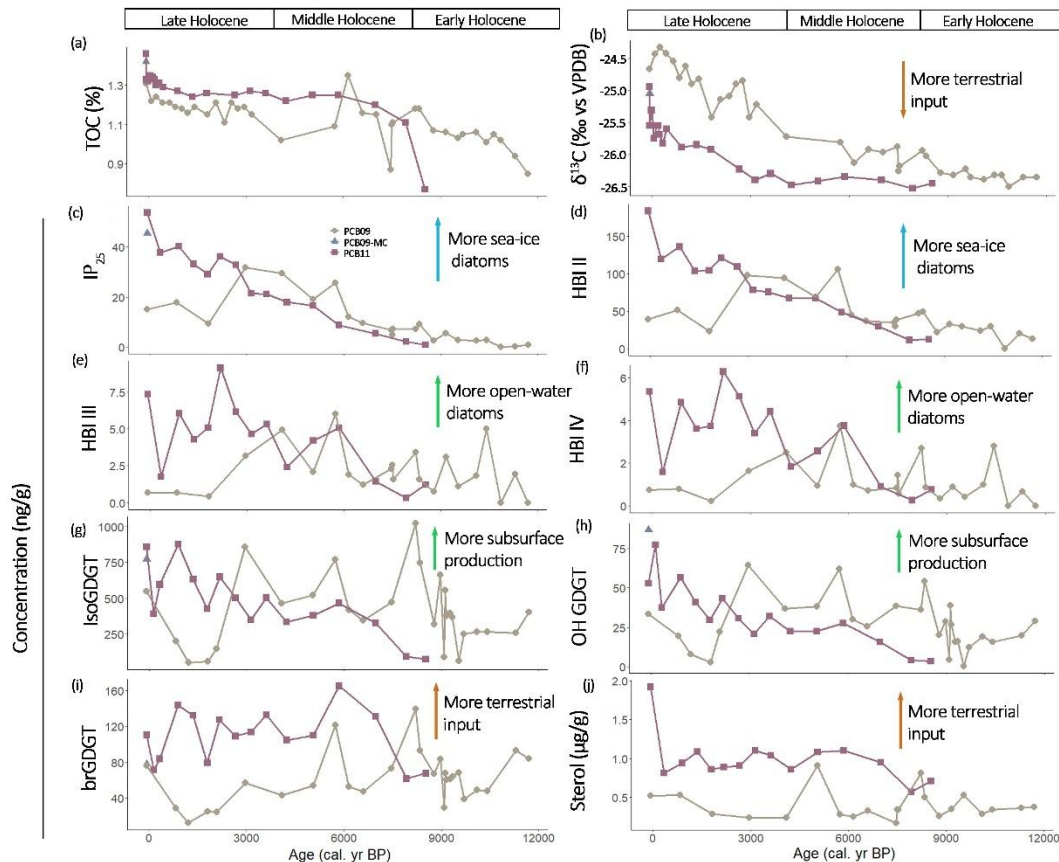
Figure 3: Bulk characteristics and biomarker concentrations (in ng/gs$_{ediment}$) for core PCB09 (brown circles) and
PCB11 (red squares) with (a) total Organic Carbon (TOC), (b) δ^{13}C, (c) IP$_{25}$, (d) HBI-II, (e) HBI III, (f) HBI IV, (g)
isoprenoid GDGTs (isoGDGT), (h) hydroxylated GDGTs (OH-GDGT), (i) branched GDGTs (brGDGT) and (j)
terrestrial sterols (sum of brassicasterol, stigmasterol, β-sitosterol, campesterol).

3.2. Lipid biomarkers

IP$_{25}$ and HBI II (C$_{25:2}$) concentrations were generally low (< 2 ng/g) in the Early Holocene (Fig. 3c,d). IP$_{25}$ in both

cores increased throughout the Middle to Late Holocene. During the Late Holocene, IP$_{25}$ and HBI II concentrations

dropped in PCB09 around 1.8 ± 1.5 ka. Concentrations of both biomarkers were higher in PCB11 than in PCB09

after 3 ka, reaching modern values of 40 ng g^{-1} and 150 ng g^{-1} (IP$_{25}$ and HBI II). PIP$_{25}$ values in both cores increased

from the Early to the Mid-Holocene (Fig. 4a).

HBI III (C$_{25:3}$) and HBI IV (C$_{25:4}$) were low in both cores with values below 8 ng g^{-1} (Fig. 3e,f). Concentrations were

higher in PCB11 than in PCB09 after 4 ka

301   The concentration of isoGDGTs and OH-GDGTs followed a similar pattern throughout the Holocene (Fig. 3g,h).

302   IsoGDGTs and OH-GDGT concentrations in PCB09 were stable during the Early Holocene at around 400 ng g^{-1} and

303   25 ng g^{-1}, respectively. At around 8.5 ka, the isoGDGTs and OH-GDGT amounts doubled. Throughout the Mid-

304   Holocene, isoGDGTs and OH-GDGT concentrations were variable but above 500 ng g^{-1}. A drop in PCB09 to almost

305   below detection limits occurred between 1-1.5 ka. IsoGDGTs and OH-GDGTs in PCB11 showed a steady increase

306   from around 100 ng g^{-1} and 10 ng g^{-1}, respectively, in the Early Holocene to >500 ng g^{-1} and >50 ng g^{-1} (Fig. 3g,h).

307   BrGDGTs concentrations in PCB09 were below 100 ng g^{-1} throughout the cores except for peaks during the Early

308   and Mid-Holocene at 11.2 ± 0.3, 8.2 ± 0.5 and 5.7 ± 0.5 ka, the latter was also seen in PCB11 (albeit concentrations

309   were higher in PCB11) (Fig. 3i). BIT values varied from 0.1 to 0.4 in PCB09 and from 0.1 and 0.5 in PCB11. The

310   #$ring_{tetra}$ values were always < 0.7 for both cores. Terrestrial sterol concentrations in PCB09 were relatively stable

311   throughout the core except for short-lived peaks at 9.5 ± 0.4, 8.2 ± 0.5 and 5.0 ± 0.9 ka (Fig. 3j). In PCB11, the

312   concentration remained stable throughout the core after an initial increase at 6.9 ± 0.6 ka and a peak in the surface

313   sediment.

314   Although biomarker concentrations expressed per gram of sediment may be influenced by mineral dilution or post-

315   depositional degradation, TOC contents in our cores varied only slightly (0.9-1.3 % in PCB09 and 1.1-1.3 % in

316   PCB11; Figure 3a). Such limited variability indicates that TOC normalization would not substantially alter the

317   observed trends. The distinct downcore patterns among lipid biomarker classes therefore likely reflect differences in

318   source input and preservation rather than a uniform effect of degradation or dilution.

319   **3.5. Salinity, SST and terrestrial input inferred from biomarker ratios**

320   Surface sediments δ^2H $C_{16:0}$ values from the Beaufort Sea (Fig. S1, S4) range from -275 to -200‰, comparable with

321   the values obtained by the preliminary study of Sachs et al. (2018). δ^2H $C_{16:0}$ values of all sediments correlate with

322   summer salinity ($r^2 = 0.63$, $p < 0.001$) and the calibration equation is the same as the one obtained by Sachs et al.

323   (2018). It is to be noted that the uncertainty associated with the analysis and calibration reaches 7 psu, which is quite

324   large for salinity changes over glacial-deglacial timescales. This is to the contrary to what Allan et al. (2023) and J.

325   Wu et al. (2025) observed in a set of surface sediments in Baffin Bay and a downcore record of the Beaufort Sea,

326   where no relationship with salinity is observed. This contrast for the surface sediments could come from the different

327   environment as Baffin Bay is a much more enclosed basin compared to the Beaufort Sea, or that δ^2H $C_{16:0}$ values

328   encompassed a too small range of salinity (28 – 34 psu). The downcore Beaufort Sea record yielded no notable salinity

329   response of the δ^2H $C_{16:0}$ when large freshwater influence were expected, which was attributed to the production of

330    $C_{16:0}$ by heterotrophs (J. Wu et al., 2025).

331   Sea surface salinity inferred from δ^2H $C_{16:0}$ values at PCB09 increased from 27 psu ± 7 during the Early Holocene to

332   30 ± 7 psu during the Mid-Holocene, and remained stable until 3 ka, increasing to 32 ± 7 psu during the Late Holocene

333   (Fig. 4b). Reconstructed salinity at PCB11 was more stable during the Mid-Holocene and Late Holocene (28 ± 7 psu)

334   until an increase to 30 ± 7 psu in the last centuries. (Fig. 4b). Although uncertainties associated with reconstructed

335   salinity are large (± 7 psu) the salinity trend between both locations agree with modern observations of lower salinities

336   at PCB11 than further offshore at PCB09 (Fig. S2).

337   Two different sets of SSTs were reconstructed using the OH-GDGT only (RI-OH') or a combination of OH- and

338   isoGDGT (TEX-OH) (Fig. 4d, Fig. S4, S5a,b). SSTs were only reconstructed when the BIT index was below 0.3 (Fig.

339   4c) as both calibrations are sensitive to terrestrial input (Varma et al., 2025). RI-OH' in the surface sediments varies

340   from 0.05 to 0.17 while TEX-OH varies from 0.08 to 0.32. Both indexes plot in the global calibration curves from

341   (Varma et al., 2024) and the reconstructed SST varies from 0.9 to 4.0 °C and -0.1 to 11.6 °C, respectively. TEX-OH

342   reconstructed SSTs in PCB09 varied between 7 ± 2.6°C in the Early Holocene, remained stable during the Mid-

343   Holocene (~3± 2.6°C), decreased to 0 ± 2.6°C between 1-1.5 ka and after which they increase to 5 ± 2.6°C, close to

344   modern summer SST (Locarnini et al., 2024). The reconstructed SST in the multicore is -1 ± 2.6°C, similar, within

345   the calibration error, to modern annual SST (Locarnini et al., 2024) (Fig. 4d). RI-OH' reconstructed SSTs in PCB09

346   produce high temperatures (~12 ± 2.6°C) between 7 and 10 ka, maybe due to non-thermal impact on the production

347   of OH-GDGT (Harning & Sepúlveda, 2024). For both cores, reconstructed SST using RI-OH' is stable around 3 °C

348   (Fig. S5b). PCB11 TEX-OH reconstructed SSTs are stable during the Early to Mid-Holocene (~5.0±2.6°C). However,

349   after 1 ka the reconstruction produces unrealistically large variation (5-15°C, Fig. S5a).

350   The BIT index showed a steady decrease in PCB11 throughout the Holocene and until 3 ka in PCB09 (Fig. 4c). In

351   PCB09, this decrease was interrupted at 9 ka and at 1.5 ka with BIT index values reaching 0.3 and 0.4, respectively.

352   The increase at 9 ka was likely due to a relative decrease in crenarchaeol concentration (Fig. S5a) whereas the 1.5 ka

353   increase was likely due to a decrease in brGDGT concentration (Fig. 4i).

354
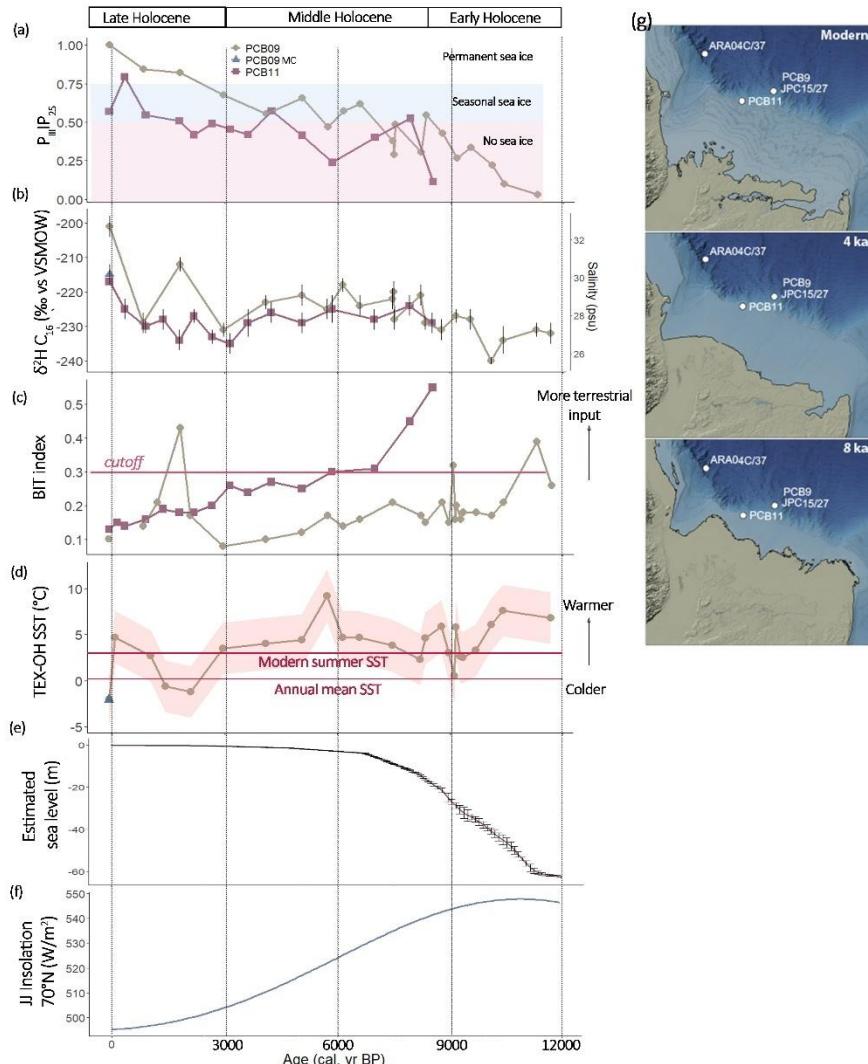
Figure 4: Reconstructed environmental parameters for PCB09 (brown circles) and PCB11 (red squares) (a) $P_{III}IP_{25}$ (PIP$_{25}$ calculated with HBI III as phytoplankton biomarker), (b) δ^2H of $C_{16:0}$ fatty acid and corresponding reconstructed salinity (Sachs et al., 2018), (c) BIT index (Hopmans et al., 2004), (d) SST derived from TEX-OH (Varma et al., 2024) shaded areas indicate the uncertainties of the reconstruction, modern (1995-2004) annual and summer SSTs were extracted from (Locarnini et al., 2024) (e), global sea level estimates derived from Lambeck et al., (2014) and (f) 21 June insolation at 70°N (Laskar et al., 2004). Panel g) Illustrative examples of plaeoshorelines at 8 and 4 ka compared to the modern. These were generated by adjusting the sea-level using the modern bathymetry portrayed in IBCAO V. 5 (Jakobsson et al., 2024). Relative sea-level adjustments were taken from ICE 6G_C (Peltier et al., 2015) for the grid cell encompassing the position of PCB11. The sea-level adjustments for this location were 46 m at 8 ka and 12 m at 4 ka (Figure S7).

365

3.6. Micropaleontology

367 Almost all of the planktonic foraminifera (99-100% in abundance relative to other species) observed in PCB09 are *N.*

368 *pachyderma*, formerly *N. pachyderma sinistra*. This is expected since this species has been found to dominate polar

369 water masses (e.g. Eynaud 2011; Moller, Schulz, and Kucera 2013). Planktonic foraminifera are mostly absent in

370 PCB11, consistent with data from plankton tows indicating that planktic foraminifera are rare on the Canadian shelf

371 where surface waters are influenced by Mackenzie River discharge (Vilks, 1989). In PCB09, the foraminiferal shells

372 appear white and fragmented in sections with abundant light-colored and sand-sized ice-rafted debris and other detrital

373 materials (Fig. S6). Foraminifera are more abundant in samples that have relatively more mud aggregates than sand-

374 sized debris (Fig. 2a,b). There is almost zero accumulation rate (per mm yr^{-1}) of *N. pachyderma* within the shelf slope

375 from 10 ka.

376 **4. Discussion**

377 This study aims to reconstruct Holocene paleoenvironmental conditions in the southeastern Beaufort Sea focusing on

378 spatial variability between the shelf slope (> 500 m water depth) and the outer shelf (<100 m water depth). By analyzing

379 the abundance and ratios of sea ice biomarkers (IP$_{25}$, HBI II), phytoplankton and heterotrophic archaeal productivity

380 markers (HBI III, HBI IV, iso- and OH-GDGT), terrestrial inputs (brGDGTs, terrestrial sterols), and reconstructed

381 environmental indicators (salinity, SST) this study aim to highlight spatial environmental difference between a shallow

382 (PCB11) and deep (PCB09) site. In the following sections, we interpret biomarker records in a chronological

383 framework, highlighting the dynamic relationship between freshwater inputs, ocean circulation, and sea ice conditions.

384 **4.1. Late glacial to Early Holocene (12 – 8.2 ka)**

385 The Late glacial to Early Holocene is only recorded at the shelf slope location (PCB09, Fig. 1). This period is

386 characterized by low concentrations of sea ice biomarkers (Fig. 3a,b) resulting in low PIP$_{25}$ values (Fig. 4a). The low

387 concentration suggests that this area had intermittent sea ice coverage during the Late glacial to Early Holocene, but

388 the presence of HBI III and HBI IV (Fig. 3e,f) indicate that the region was only under seasonal ice cover until spring

389 allowing late spring/summer open-water diatom primary production (Belt et al., 2015). Heterotrophic production in

390 the shelf slope region during this period is relatively low (as suggested by the presence of ammonium oxidizer

391 Thaumarchaea-derived isoGDGTs, Schouten et al., 2013, Fig. 3g, h) but increased and peaked at 8.2 ± 0.5 ka. During

392 12 – 8.2 ka, SSTs were elevated in comparison with the rest of the Holocene (Fig. 4d) which coincided with peak 21

393 June insolation (Fig. 4f) (Clemens et al., 2010; Laskar et al., 2004). The warmer surface waters might have inhibited

394 the development of sea ice over the Beaufort Shelf.

395   During the Late glacial to Early Holocene, large freshwater inputs to the Beaufort Shelf, inferred from the low

396   reconstructed salinity (Fig. 4b) likely originated from the decaying Laurentide Ice Sheet. Such water masses derived

397   from drainage regions that had undergone minimal weathering would have released low amounts of nutrients. The

398   influx of low-salinity freshwater may have intensified salinity-driven stratification on the shelf, reducing the upwelling

399   of nutrient-rich saline Pacific waters to the surface which also limited nutrient availability. This stratification and

400   lower nutrient availability likely limited primary productivity and the presence of ammonia-oxidizers on the Beaufort

401   Shelf. It is important to note that sea level on the Beaufort Shelf was >60 m lower in the Early Holocene than it is

402   today (Fig. 4e). Implying that between 10-12 ka, the Beaufort Sea was a shallow estuarine environment (Fig. 4g, Hill

403   et al., 1993).

404   The concentration of brGDGTs and terrestrial sterols in the shelf slope location during the Early Holocene peaked at

405   11.3 ± 0.3 and 8.2 ± 0.5 ka (Fig. 3i,j), which agrees with meltwater outflow from the LIS and freshly deglaciated

406   surfaces as seen in nearby cores (Klotsko et al., 2019; J. Wu et al., 2020). Additionally, increased freshwater input

407   may have transported more detrital calcium (Ca), as indicated by elevated Ca/Ti ratios (Fig. 2a), which could have

408   enhanced the preservation of foraminifera by buffering the water column and limiting carbonate dissolution, in

409   sediments along the shelf slope. Murton et al. (2010) used optically stimulated luminescence (OSL) dating to identify

410   two major meltwater pulses through the Mackenzie River system between 13 and 11.7 ka and between 11.7 and 9.3

411   ka. This timing is supported by sedimentary and isotopic records from the Beaufort Sea indicating a major Lake

412   Agassiz flood route through the Mackenzie system (Keigwin et al., 2018; Klotsko et al., 2019). These meltwater events

413   coincide with events (11.3 ± 0.3, 8.2 ± 0.5 ka) in the biomarker records from this study (Fig. 3), and one event at 10.1

414   ± 0.4 ka is recorded in the reconstructed salinity (Fig. 4b), suggesting enhanced freshwater forcing impacted ocean

415   circulation and increased sea ice extent. The massive meltwater discharge from the LIS (at least $\sim$9000 km³) into its

416   surrounding oceans has been the major cause for eustatic sea level rise from 10 to 6 ka (Moran & Bryson, 1969).

417   **4.2. Middle to Late Holocene (8.2 – 0 ka)**

418   After 8.2 ka, environmental conditions at the shelf slope (PCB09) and the outer shelf (PCB11) diverged markedly,

419   reflecting their contrasting depositional and oceanographic settings. At PCB09, SSTs cooled from ~6 °C to 3 °C (Fig.

420   4d), while steadily increasing sea-ice biomarker concentrations led to $PIP_{25} > 0.5$ by 7-6 ka, indicating the

421   establishment of stable ice-edge or polynya conditions at the slope. The higher salinity (Fig. 4b) and greater distance

422   from the coast at this site suggest enhanced influence of offshore Pacific-derived waters and reduced terrestrial input.

423   In contrast, at the outer shelf site PCB11, sea-ice biomarkers also increased after 8.5 ka but were accompanied by

424   persistently high concentrations of open-water diatom markers, implying continued seasonal sea-ice and productive

425   flaw-lead conditions, i.e., an open-water or newly formed sea-ice zone between landfast ice and sea ice. The flaw-lead

426   today occurs about 80 km away from shore (Fig. S1) (Carmack et al., 2004). The proximity of PCB11 to the coastline

427   before 6 ka (Fig. 4g) likely favored landfast-ice diatom assemblages and greater sensitivity to freshwater discharge.

428   Only after 4 ± 0.5 ka did PCB11 reach PIP_{25} values comparable to the slope, indicating a delayed transition to stable

429   seasonal sea ice, approximately 2 kyr later than at PCB09. Thus, while both sites record a Middle-Holocene trend

430   toward increasing sea-ice cover, the slope experienced earlier stabilization and reduced productivity linked to offshore

431   cooling and stratification, whereas the outer shelf remained a dynamic, seasonally open-water environment likely

432   sustained by coastal flaw-lead formation, and strong riverine influence.

433   In the Late Holocene (4.2 ka to present), the two Beaufort sites again show distinct sea-ice and productivity trajectories

434   reflecting their different hydrographic settings. At the slope site, perennial sea ice cover developed after 3 ka as

435   indicated by higher PIP_{25} values (>0.8), increased reconstructed salinity (Fig. 4a,b), as well as a decline in open-water

436   diatom biomarkers (Fig. 3e,f). A sharp decrease in PIP_{25} and open-water diatom biomarkers at 1.5 ± 1.5 ka suggests a

437   shift to year-round ice cover coincident with low SST (~0 °C, Fig. 4d). The parallel reduction in heterotrophic archaeal

438   production may reflect strengthened water-column stratification or reduced nutrient supply, consistent with restricted

439   shelf-break upwelling (Schulze & Pickart, 2012). These changes are broadly consistent with the timing of the regional

440   cooling associated with the Little Ice Age (Mann et al., 2009), although the resolution of the biomarker record does

441   not allow precise attribution to centennial-scale events. In contrast, on the outer shelf, seasonal sea-ice conditions

442   persisted longer and sea ice cover expanded gradually and became well established after about 2 ± 0.6 ka. Even as

443   sea-ice biomarkers increased, open-water diatom markers remained relatively abundant, implying continued flaw-lead

444   or marginal-ice-zone productivity sustained by intermittent open-water formation and coastal influence.

445   By the last 0.4 ka, both sites reached modern configurations, but with clear spatial differences: PCB09 records

446   persistently thick, multi-year ice and limited primary production, whereas PCB11 retains higher concentrations of

447   both sea-ice and open-water diatom biomarkers, consistent with modern flaw-lead dynamics observed near the outer

448

shelf (Fig. S1).
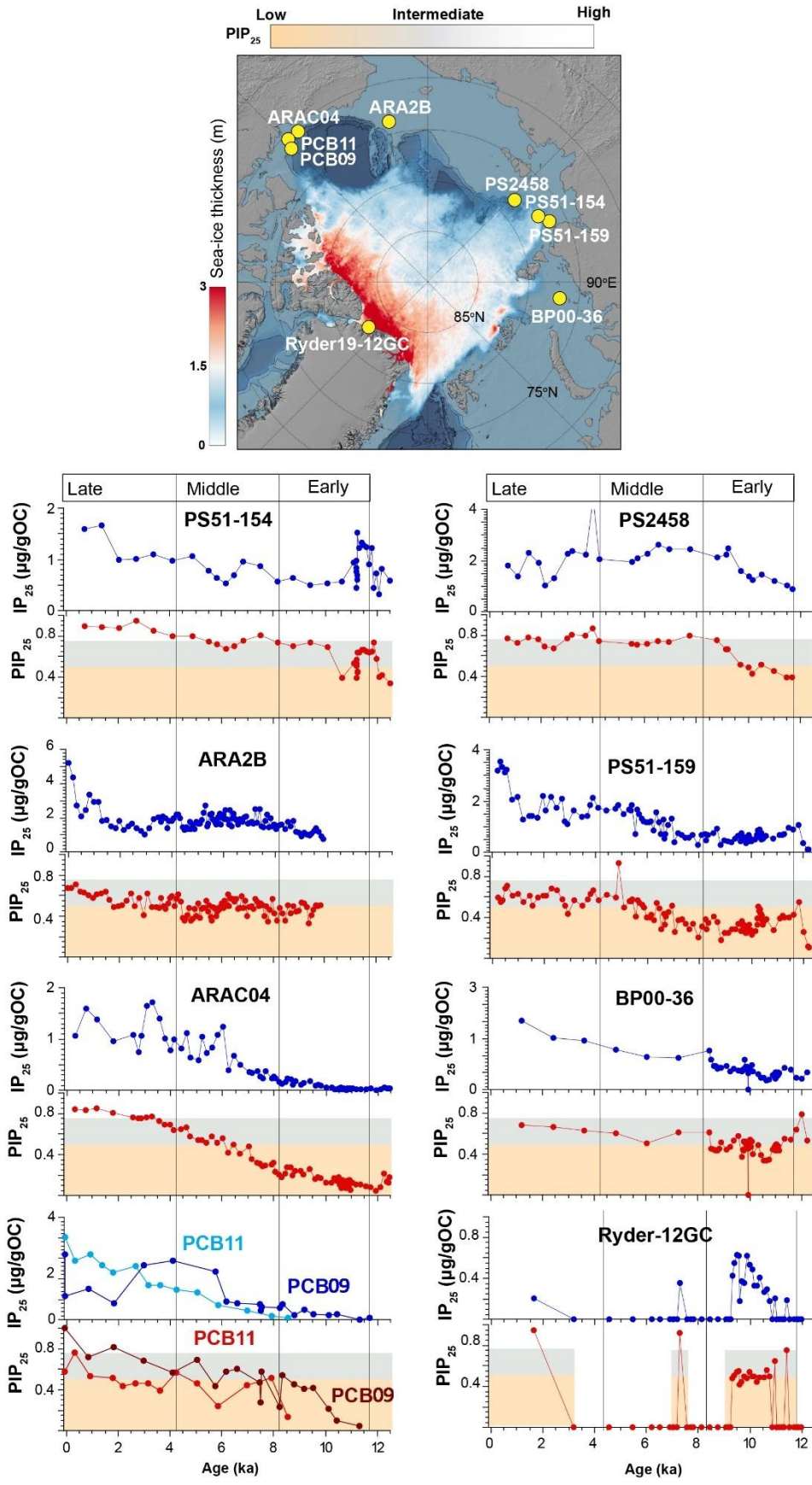
449 Figure 5: Arctic sea-ice records (PIP_{25} and IP_{25} concentration) covering the Holocene: PCB (this study), ARAC04 *(J.*
450 *Wu et al., 2020)*, ARA2B (Stein et al., 2017), PS51-154 and PS51-159 (Hörner et al., 2016), PS5428 (Fahl & Stein,
451 2012), BP0036 (Hörner et al., 2018), Ryder19-12 (Detlef et al., 2023). Average thickness of sea ice (in meters) for
452 September 2023. Data from the Arctic Ocean Sea Ice Reanalysis (Williams et al., 2021) obtained via the E.U.
453 Copernicus Marine Service Information MyOcean Viewer (https://marine.copernicus.eu/access-data/myocean-
454 viewer).The shaded rectangles indicate the limit of the proxy for no sea-ice in red, seasonal sea ice in blue
455 ($0.5<PIP_{25}<0.75$) and permanent sea ice above $PIP_{25} > 0.75$.

456 **4.3. Comparison with other Arctic marginal seas**

457 Previous studies using IP_{25} to reconstruct sea ice variability in Arctic marginal seas have reported largely open-water

458 conditions with significant freshwater influence during the Late glacial to Early Holocene.

459 The nearby cores JPC15 (Keigwin et al., 2018), ARAC20 (J. Wu et al., 2020) (Fig. 1) recorded similar environmental

460 changes (sea ice cover, freshwater input) as in PCB09 but different from those recorded in the shallow PCB11 site,

461 highlighting the differences between shelf slope and outer shelf and the spatial variation of the polynya position. Aside

462 from the close-by cores (Keigwin et al., 2018; Klotsko et al., 2019; J. Wu et al., 2020), other Arctic records in the

463 Canadian Archipelago (Vare et al., 2009), East Siberian (Dong et al., 2022), Kara (Hörner et al., 2018) , Chukchi

464 (Stein et al., 2017), Laptev (Fahl & Stein, 2012; Hörner et al., 2016), and Lincoln (Detlef et al., 2023) Seas and along

465 the Lomonosov Ridge (Stein & Fahl, 2012), report minimum sea-ice cover during the Early Holocene (centered around

466 10 ka) (Fig. 5). Detlef et al. (2023) reconstructed sea ice conditions from a sediment core covering the last 11 ka,

467 showing that while the Lincoln Sea currently experiences perennial sea ice cover ($PIP_{25} = 0$), it underwent a shift to

468 seasonal sea ice during the Early Holocene (around 10 ka) due to significantly warmer conditions ($PIP_{25} > 0.5$). This

469 period of reduced sea ice cover is associated with increased marine productivity and meltwater input indicated by

470 biomarker and sedimentary facies. The Northern Greenland (Detlef et al., 2023) and the site offshore the Laptev Sea

471 on the Lomonosov Ridge (Fahl & Stein, 2012; Hörner et al., 2016) are the first regions to record permanent sea-ice

472 cover beginning around 9 ka after the Early Holocene minimum. The Beaufort Sea (this study, J. Wu et al., 2020)

473 showed permanent sea-ice cover over the slope after 3 ka. Seasonal sea-ice cover in the shallower regions of the

474 Laptev and Beaufort Seas (PS51-159 and PCB11) was developed after 5 and 3 ka, respectively. The Chukchi Sea

475 (ARA2B) had seasonal sea-ice from the Mid-Holocene onwards, with an increase after 4.5 ka (Stein et al., 2017). The

476 variations in sea ice cover and primary production in the Chukchi Sea were attributed to differences in solar insolation

477 and variability in Pacific water inflow, which brought increased heat flux and episodic declines in sea ice cover. In

478 the Canadian Archipelago, a record that did not include the Early Holocene, (Belt et al., 2010; Vare et al., 2009)

479 increased sea-ice cover exists from from 7 to 3 ka.

480   In contrast, studies using dinocyst assemblages from around the Arctic Ocean (see the review of de Vernal et al., 2013)

481   report constant sea ice cover for the Early to Mid-Holocene with a clear decrease around 6 ka, followed by a return to

482   pre-6 ka conditions until an increase toward modern times. This could be due to a warm-bias in the dinocyst estimate

483   or a non-representative training set (de Vernal et al., 2013).

484   Together, many of the biomarker studies provide a consistent narrative of spring sea ice development during the

485   Holocene across the Arctic Ocean following a period of high insolation in the Early Holocene. The transition from

486   largely open-water and freshwater-influenced conditions during the Late glacial to Early Holocene to increasing sea

487   ice cover from the Mid-Holocene onward is a shared feature across the Arctic shelf seas, although regional variations

488   in sea ice dynamics and productivity are observed due to local freshwater input and oceanographic conditions.

489   Evidence from areas with permanent sea ice, such as the Lincoln Sea, shows that the minimum ice cover during the

490   Late glacial extended even into the high Arctic, offering insights into the extent of sea ice reduction during this time.

491   **5. Conclusions**

492   Analysis of two sediment cores from the outer Beaufort Shelf and shelf slope help elucidate the region's

493   paleoenvironmental variability throughout the Holocene. The shelf slope experienced ice-free to minimal sea ice

494   extent during the Late glacial and Early Holocene. During the Early Holocene, the Beaufort Shelf was ~60 m shallower

495   than today, and experienced large freshwater influxes due to the decaying LIS. The following sea level rise brought

496   the core sites further away from the river mouth and eroding permafrost coasts, lowering the input of terrestrial organic

497   matter. Cooling during the Mid-Holocene drove an increase in sea ice cover for the Beaufort Shelf and other Arctic

498   marginal seas. Sea-ice cover and its impact on local upwelling and regional Pacific inflow impacted local primary

499   production, concentrating the phytoplankton production in open-water flaw-lead or polynya conditions. Open water

500   conditions substantially decreased during the Late Holocene as extended sea ice cover developed at the shelf slope,

501   which caused primary productivity to further decline. This study highlights broadly consistent patterns of sea ice

502   variability across Arctic marginal seas, implying similar controls on sea-ice dynamics, and underscoring the

503   vulnerability of perennial sea-ice as contemporary climate conditions reach or surpass those from the Early Holocene.

504   **Data availability**

505 The research data are published on the Bolin Center database 10.17043/lattaud-2025-sediment-beaufort-surface-1 and

506 10.17043/lattaud-2025-sediment-beaufort-1.

507 **Author contribution** MS - Data Curation, Formal analysis, Investigation, Writing – original draft preparation, LBr

508 Conceptualization, Supervision, Funding acquisition, Writing – review & editing, MO Resource, Funding acquisition,

509 Investigation, Writing – review & editing IH Conceptualization, Supervision, Writing – review & editing, TT

510 Resource, Writing – review & editing LBi Investigation, NH Resource, Writing – review & editing, DN Resource,

511 Writing – review & editing, MF Funding acquisition, Writing – review & editing, JL Conceptualization, Funding

512 acquisition, Investigation, Project administration, Supervision, Writing – review & editing

513 **Competing interest** The authors declare that they have no conflict of interest.

514 **Acknowledgments**

515 We thank Amundsen Science and ArcticNet for their support in preparing the cruise and the crew of the CCGS

516 Amundsen and the PeCaBeau team for their help during sampling. We thank the Alfred Wegener Institute for

517 providing the multicorer and part of the logistical support. Carina Johansson is thanked for her help with XRF analysis,

518 and Axel Birkholz and Thomas Kuhn for the bulk elemental and isotopic analysis. MS was funded through a SNSF-

519 Ambizione (PZ00P2-209012) to JL. The ship-time leading to sample acquisition for this study was funded by the

520 European Union H2020 as part of the EU Project ARICE (grant agreement n° 730965) with additional support from

521 the Swiss Polar Institute (Project number PAF-2020-004).

522

523   **References**

524   Belt, Simon T., Guillaume Massé, Steven J. Rowland, Michel Poulin, Christine Michel, and Bernard LeBlanc. 2007.

525   "A Novel Chemical Fossil of Palaeo Sea Ice: IP_{25}." *Organic Geochemistry* 38 (January): 16–27.

526   https://doi.org/10.1016/j.orggeochem.2006.09.013.

527   Belt, Simon T., and Juliane Müller. 2013. "The Arctic Sea Ice Biomarker IP_{25}: A Review of Current Understanding,

528   Recommendations for Future Research and Applications in Palaeo Sea Ice Reconstructions." *Quaternary Science*

529   *Reviews* 79 (November): 9–25. https://doi.org/10.1016/j.quascirev.2012.12.001.

530   Broecker, Wallace S., James P. Kennett, Benjamin P. Flower, James T. Teller, Sue Trumbore, Georges Bonani, and

531   Willy Wolfli. 1989. "Routing of Meltwater from the Laurentide Ice Sheet During the Younger Dryas Cold Episode."

532   *Nature* 341 (September): 318–21. https://doi.org/10.1038/341318a0.

533   Brown, T. A., S. T. Belt, A. Tatarek, and C. J. Mundy. 2014. "Source Identification of the Arctic Sea Ice Proxy IP_{25}."

534   *Nature Communications* 5 (June): 4197. https://doi.org/10.1038/ncomms5197.

535   Buizert, Christo, Vasileios Gkinis, Jeffrey P. Severinghaus, Feng He, Benoit S. Lecavalier, Philippe Kindler, Markus

536   Leuenberger, et al. 2014. "Greenland Temperature Response to Climate Forcing During the Last Deglaciation."

537   *Science* 345 (September): 1177–80. https://doi.org/10.1126/science.1254961.

538   Carlson, Anders E., Allegra N. LeGrande, Delia W. Oppo, Rosemarie E. Came, Gavin A. Schmidt, Faron S. Anslow,

539   Joseph M. Licciardi, and Elizabeth A. Obbink. 2008. "Rapid Early Holocene Deglaciation of the Laurentide Ice

540   Sheet." *Nature Geoscience* 1 (9): 620–24. https://doi.org/10.1038/ngeo285.

541   Carmack, EC, RW Macdonald, and S Jasper. 2004. "Phytoplankton Productivity on the Canadian Shelf of the Beaufort

542   Sea." *Marine Ecology Progress Series* 277: 37–50. https://doi.org/10.3354/meps277037.

543   Dai, Aiguo, Dehai Luo, Mirong Song, and Jiping Liu. 2019. "Arctic Amplification Is Caused by Sea-Ice Loss Under

544   Increasing CO2." *Nature Communications* 10 (January): 121. https://doi.org/10.1038/s41467-018-07954-9.

545   Data, I. E. 2021) National Snow and Ice Data Center. https://nsidc.org/

546   Detlef, Henrieka, Matt O'Regan, Christian Stranne, Mads Mørk Jensen, Marianne Glasius, Thomas M. Cronin, Martin

547   Jakobsson, and Christof Pearce. 2023. "Seasonal Sea-Ice in the Arctic's Last Ice Area During the Early Holocene."

548   *Communications Earth & Environment* 4 (1). https://doi.org/10.1038/s43247-023-00720-w.

549   Eicher, O.; Baumgartner, M.; Schilt, A.; Schmitt, J.; Schwander, J.; Stocker, T.F.; Fischer, H. (2016-10-06):

550   NOAA/WDS Paleoclimatology - NGRIP Ice Core 120,000 Year Total Air Content Data. [indicate subset used].

551   NOAA National Centers for Environmental Information. https://doi.org/10.25921/n0d0-ng26. Accessed [July 2023].

552   Eynaud, Frédérique. 2011. "Planktonic Foraminifera in the Arctic: Potentials and Issues Regarding Modern and

553   Quaternary Populations." *IOP Conference Series: Earth and Environmental Science* 14 (May): 012005.

554   https://doi.org/10.1088/1755-1315/14/1/012005.

555   Fietz, Susanne, Sze Ling Ho, and Carme Huguet. 2020. "Archaeal Membrane Lipid-Based Paleothermometry for

556   Applications in Polar Oceans." *Oceanography* 33 (June). https://doi.org/10.5670/oceanog.2020.207.

557   Frey, K. E., J. C. Comiso, L. W. Cooper, J. M. Grebmeier, and L. V. Stock. 2020. "Arctic Ocean Primary Productivity:

558   The Response of Marine Algae to Climate Warming and Sea Ice Decline - NOAA Arctic — Arctic.noaa.gov."

559   https://arctic.noaa.gov/Report-Card/Report-Card-2020/ArtMID/7975/ArticleID/900/Arctic-Ocean-Primary-

560   Productivity-The-Response-of-Marine-Algae-to-Climate-Warming-and-Sea-Ice-Decline.

561   Häkkinen, Sirpa. 1987. "Upwelling at the Ice Edge: A Mechanism for Deep Water Formation?" *Journal of*

562   *Geophysical Research* 92 (C5): 5031. https://doi.org/10.1029/jc092ic05p05031.

563   Hartman, Julian D., F. Sangiorgi, M. A. Barcena, F. Tateo, F. Giglio, S. Albertazzi, F. Trincardi, P. K. Bijl, L. Langone,

564   and A. Asioli. 2021. "Sea-Ice, Primary Productivity and Ocean Temperatures at the Antarctic Marginal Zone During

565   Late Pleistocene." *Quaternary Science Reviews* 266 (August): 107069.

566   https://doi.org/10.1016/j.quascirev.2021.107069.

567   Herfort, Lydie, Stefan Schouten, Ben Abbas, Marcel J. W. Veldhuis, Marco J. L. Coolen, Cornelia Wuchter, Jan P.

568   Boon, Gerhard J. Herndl, and Jaap S. Sinninghe Damste. 2007. "Variations in Spatial and Temporal Distribution of

569   Archaea in the North Sea in Relation to Environmental Variables." *FEMS Microbiology Ecology* 62 (3): 242–57.

570   https://doi.org/10.1111/j.1574-6941.2007.00397.x.

571 Hill, Philip R., Arnaud Héquette, and Marie-Hélène Ruz. 1993. "Holocene Sea-Level History of the Canadian Beaufort

572 Shelf." *Canadian Journal of Earth Sciences* 30 (1): 103–8. https://doi.org/10.1139/e93-009.

573 Huguet, C., Kim, J., Sinninghe Damsté, J. S., and Schouten, S. 2006: Reconstruction of sea surface temperature

574 variations in the Arabian Sea over the last 23 kyr using organic proxies (TEX86 and U37K′), Paleoceanography, 21,

575 https://doi.org/10.1029/2005pa001215.

576 Hopmans, Ellen C, Johan W. H Weijers, Enno Schefuß, Lydie Herfort, Jaap S Sinninghe Damsté, and Stefan Schouten.

577 2004. "A Novel Proxy for Terrestrial Organic Matter in Sediments Based on Branched and Isoprenoid Tetraether

578 Lipids." *Earth and Planetary Science Letters* 224 (July): 107–16. https://doi.org/10.1016/j.epsl.2004.05.012.

579 Kashiwase, Haruhiko, Kay I. Ohshima, Sohey Nihashi, and Hajo Eicken. 2017. "Evidence for Ice-Ocean Albedo

580 Feedback in the Arctic Ocean Shifting to a Seasonal Ice Zone." *Scientific Reports* 7 (August): 8170.

581 https://doi.org/10.1038/s41598-017-08467-z.

582 Keigwin, L. D., S. Klotsko, N. Zhao, B. Reilly, L. Giosan, and N. W. Driscoll. 2018. "Deglacial Floods in the Beaufort

583 Sea Preceded Younger Dryas Cooling." *Nature Geoscience* 11 (8): 599–604. https://doi.org/10.1038/s41561-018-

584 0169-6.

585 Lake, Robert Alan. 1967. "Heat Exchange Between Water and Ice in the Arctic Ocean." *Archiv Für Meteorologie,*

586 *Geophysik Und Bioklimatologie Serie A* 16 (October): 242–59. https://doi.org/10.1007/BF02246401.

587 Laskar, J., P. Robutel, F. Joutel, M. Gastineau, A. C. M. Correia, and B. Levrard. 2004. "A Long-Term Numerical

588 Solution for the Insolation Quantities of the Earth." *Astronomy & Astrophysics* 428 (December): 261–85.

589 https://doi.org/10.1051/0004-6361:20041335.

590 Lattaud, J., Bröder, L., Haghipour, N., Rickli, J., Giosan, L., and Eglinton, T. I. 2021. Influence of Hydraulic

591 Connectivity on Carbon Burial Efficiency in Mackenzie Delta Lake Sediments, Journal of Geophysical Research:

592 Biogeosciences, 126. https://doi.org/10.1029/2020jg006054.

593 Leri, A. C., Mayer, L. M., Thornton, K. R., and Ravel, B. 2014. Bromination of marine particulate organic matter

594 through oxidative mechanisms, Geochimica et Cosmochimica Acta, 142, 53–63,

595 https://doi.org/10.1016/j.gca.2014.08.012.

596 Liu, Xiao-Lei, Julius S. Lipp, Jeffrey H. Simpson, Yu-Shih Lin, Roger E. Summons, and Kai-Uwe Hinrichs. 2012.
597 "Mono- and Dihydroxyl Glycerol Dibiphytanyl Glycerol Tetraethers in Marine Sediments: Identification of Both Core
598 and Intact Polar Lipid Forms." *Geochimica Et Cosmochimica Acta* 89 (July): 102–15.
599 https://doi.org/10.1016/j.gca.2012.04.053.

600 Lü, Jun-Mei, Seong-Joong Kim, Ayako Abe-Ouchi, Yongqiang Yu, and Rumi Ohgaito. 2010. "Arctic Oscillation
601 During the Mid-Holocene and Last Glacial Maximum from PMIP2 Coupled Model Simulations." *Journal of Climate*
602 23 (14): 3792–3813. https://doi.org/10.1175/2010jcli3331.1.

603 Lü, Xiaoxia, Xiao-Lei Liu, Felix J. Elling, Huan Yang, Shucheng Xie, Jinming Song, Xuegang Li, Huamao Yuan,
604 Ning Li, and Kai-Uwe Hinrichs. 2015. "Hydroxylated Isoprenoid GDGTs in Chinese Coastal Seas and Their Potential
605 as a Paleotemperature Proxy for Mid-to-Low Latitude Marginal Seas." *Organic Geochemistry* 89-90 (December): 31–
606 43. https://doi.org/10.1016/j.orggeochem.2015.10.004.

607 Marcott, Shaun A., Jeremy D. Shakun, Peter U. Clark, and Alan C. Mix. 2013. "A Reconstruction of Regional and
608 Global Temperature for the Past 11,300 Years." *Science* 339 (March): 1198–1201.
609 https://doi.org/10.1126/science.1228026.

610 Matero, I. S. O., L. J. Gregoire, R. F. Ivanovic, J. C. Tindall, and A. M. Haywood. 2017. "The 8.2 Ka Cooling Event
611 Caused by Laurentide Ice Saddle Collapse." *Earth and Planetary Science Letters* 473 (September): 205–14.
612 https://doi.org/10.1016/j.epsl.2017.06.011.

613 McNichol, A. P., E. A. Osborne, A. R. Gagnon, B. Fry, and G. A. Jones. 1994. "TIC, TOC, DIC, DOC, PIC, POC —
614 Unique Aspects in the Preparation of Oceanographic Samples for 14C-AMS." *Nuclear Instruments and Methods in*
615 *Physics Research Section B: Beam Interactions with Materials and Atoms* 92 (1–4): 162–65.
616 https://doi.org/10.1016/0168-583x(94)95998-6.

617 Moller, Tobias, Hartmut Schulz, and Michal Kucera. 2013. "The Effect of Sea Surface Properties on Shell Morphology
618 and Size of the Planktonic Foraminifer Neogloboquadrina Pachyderma in the North Atlantic." *Palaeogeography,*
619 *Palaeoclimatology, Palaeoecology* 391 (December): 34–48. https://doi.org/10.1016/j.palaeo.2011.08.014.

620 Moran, Joseph M., and Reid A. Bryson. 1969. "The Contribution of Laurentide Ice Wastage to the Eustatic Rise of

621 Sea Level: 10, 000 to 6, 000 BP." *Arctic and Alpine Research* 1 (2): 97. https://doi.org/10.2307/1550016.

622 Müller, Juliane, Kirstin Werner, Ruediger Stein, Kirsten Fahl, Matthias Moros, and Eystein Jansen. 2012. "Holocene

623 Cooling Culminates in Sea Ice Oscillations in Fram Strait." *Quaternary Science Reviews* 47 (July): 1–14.

624 https://doi.org/10.1016/j.quascirev.2012.04.024.

625 Murton, Julian B., Mark D. Bateman, Scott R. Dallimore, James T. Teller, and Zhirong Yang. 2010. "Identification

626 of Younger Dryas Outburst Flood Path from Lake Agassiz to the Arctic Ocean." *Nature* 464 (7289): 740–43.

627 https://doi.org/10.1038/nature08954.

628 NGRIP-Members. 2004. "High-Resolution Record of Northern Hemisphere Climate Extending into the Last

629 Interglacial Period." *Nature* 431 (7005): 147–51. https://doi.org/10.1038/nature02805.

630 Not, Christelle, and Claude Hillaire-Marcel. 2012. "Enhanced Sea-Ice Export from the Arctic During the Younger

631 Dryas." *Nature Communications* 3 (January): 647. https://doi.org/10.1038/ncomms1658.

632 Omstedt, Anders, Eddy C. Carmack, and Robie W. Macdonald. 1994. "Modeling the Seasonal Cycle of Salinity in

633 the Mackenzie Shelf/Estuary." *Journal of Geophysical Research* 99: 10011. https://doi.org/10.1029/94JC00201.

634 Park, Hyo-Seok, Seong-Joong Kim, Andrew L. Stewart, Seok-Woo Son, and Kyong-Hwan Seo. 2019. "Mid-Holocene

635 Northern Hemisphere Warming Driven by Arctic Amplification." *Science Advances* 5 (12).

636 https://doi.org/10.1126/sciadv.aax8203.

637 Pfalz, Gregor, Bernhard Diekmann, Johann-Christoph Freytag, Liudmila Syrykh, Dmitry A. Subetto, and Boris K.

638 Biskaborn. 2022. "Improving Age–Depth Relationships by Using the LANDO ('Linked Age and Depth Modeling')

639 Model Ensemble." *Geochronology* 4 (1): 269–95. https://doi.org/10.5194/gchron-4-269-2022.

640 Pickart, Robert S. 2004. "Shelfbreak Circulation in the Alaskan Beaufort Sea: Mean Structure and Variability."

641 *Journal of Geophysical Research* 109: C04024. https://doi.org/10.1029/2003JC001912.

642 Rantanen, Mika, Alexey Yu. Karpechko, Antti Lipponen, Kalle Nordling, Otto Hyvärinen, Kimmo Ruosteenoja, Timo

643 Vihma, and Ari Laaksonen. 2022. "The Arctic Has Warmed Nearly Four Times Faster Than the Globe Since."

644 *Communications Earth & Environment* 3 (August): 168. https://doi.org/10.1038/s43247-022-00498-3.

645 Richter, T. O., Gaast, S. van der, Koster, B., Vaars, A., Gieles, R., Stigter, H. C. de, Haas, H. De and Weering, T. C.E.

646 van. 2005. The Avaatech XRF Core Scanner: technical description and applications to NE Atlantic sediments, Geol

647 Soc. London, Spec. Publ., 267(1), 39–50, doi:10.1144/GSL.SP.2006.267.01.03.

648 Sachs, J. P., Stein, R., Maloney, A. E., Wolhowe, M., Fahl, K., and Nam, S.-i. 2018. An Arctic Ocean paleosalinity

649 proxy from δ2H of palmitic acid provides evidence for deglacial Mackenzie River flood events, Quaternary Science

650 Reviews, 198, 76–90, https://doi.org/10.1016/j.quascirev.2018.08.025.

651 Schouten, Stefan, Ellen C. Hopmans, and Jaap S. Sinninghe Damsté. 2013. "The Organic Geochemistry of Glycerol

652 Dialkyl Glycerol Tetraether Lipids: A Review." *Organic Geochemistry* 54 (January): 19–61.

653 https://doi.org/10.1016/j.orggeochem.2012.09.006.

654 Schouten, Stefan, Ellen C. Hopmans, Enno Schefuß, and Jaap S. Sinninghe Damsté. 2002. "Distributional Variations

655 in Marine Crenarchaeotal Membrane Lipids: A New Tool for Reconstructing Ancient Sea Water Temperatures?"

656 *Earth and Planetary Science Letters* 204 (November): 265–74. https://doi.org/10.1016/S0012-821X(02)00979-2.

657 Serreze, Mark C., and Jennifer A. Francis. 2006. "The Arctic Amplification Debate." *Climatic Change* 76 (June):

658 241–64. https://doi.org/10.1007/s10584-005-9017-y.

659 Sinninghe Damsté, Jaap S., W. Irene C. Rijpstra, Marco J. L. Coolen, Stefan Schouten, and John K. Volkman. 2007.

660 "Rapid Sulfurisation of Highly Branched Isoprenoid (HBI) Alkenes in Sulfidic Holocene Sediments from Ellis Fjord,

661 Antarctica." *Organic Geochemistry* 38 (1): 128–39. https://doi.org/10.1016/j.orggeochem.2006.08.003.

662 Smith, Richard W., Thomas S. Bianchi, and Xinxin Li. 2012. "A Re-Evaluation of the Use of Branched GDGTs as

663 Terrestrial Biomarkers: Implications for the BIT Index." *Geochimica Et Cosmochimica Acta* 80 (March): 14–29.

664 https://doi.org/10.1016/j.gca.2011.11.025.

665 Steenfelt, A., Thomassen, B., Lind, M. and Kyed, J.: Karrat. 1998. reconnaissance mineral exploration in central West

666 Greenland, Geol. Greenl. Surv. Bull., 180, 73–80.

667 Stein, Ruediger, Kirsten Fahl, Paul Gierz, Frank Niessen, and Gerrit Lohmann. 2017. "Arctic Ocean Sea Ice Cover

668 During the Penultimate Glacial and the Last Interglacial." *Nature Communications* 8 (August): 373.

669 https://doi.org/10.1038/s41467-017-00552-1.

670 Stein, Ruediger, and Robie W. MacDonald, eds. 2004. *The Organic Carbon Cycle in the Arctic Ocean*. Springer Berlin

671 Heidelberg. https://doi.org/10.1007/978-3-642-18912-8.

672 Stoll, Heather M., Isabel Cacho, Edward Gasson, Jakub Sliwinski, Oliver Kost, Ana Moreno, Miguel Iglesias, et al.

673 2022. "Rapid Northern Hemisphere Ice Sheet Melting During the Penultimate Deglaciation." *Nature Communications*

674 13: 3819. https://doi.org/10.1038/s41467-022-31619-3.

675 Teller, James T. 2013. "Lake Agassiz During the Younger Dryas." *Quaternary Research* 80: 361–69.

676 https://doi.org/10.1016/j.yqres.2013.06.011.

677 Ullman, David J., Anders E. Carlson, Steven W. Hostetler, Peter U. Clark, Joshua Cuzzone, Glenn A. Milne, Kelsey

678 Winsor, and Marc Caffee. 2016. "Final Laurentide Ice-Sheet Deglaciation and Holocene Climate-Sea Level Change."

679 *Quaternary Science Reviews* 152: 49–59. https://doi.org/10.1016/j.quascirev.2016.09.014.

680 Vernal, Anne de, Claude Hillaire-Marcel, Cynthia Le Duc, Philippe Roberge, Camille Brice, Jens Matthiessen, Robert

681 F. Spielhagen, and Ruediger Stein. 2020. "Natural Variability of the Arctic Ocean Sea Ice During the Present

682 Interglacial." *Proceedings of the National Academy of Sciences* 117: 26069–75.

683 https://doi.org/10.1073/pnas.2008996117.

684 Wu, Junjie, Ruediger Stein, Kirsten Fahl, Nicole Syring, Seung-Il Nam, Jens Hefter, Gesine Mollenhauer, and Walter

685 Geibert. 2020. "Deglacial to Holocene Variability in Surface Water Characteristics and Major Floods in the Beaufort

686 Sea." *Communications Earth & Environment* 1: 27. https://doi.org/10.1038/s43247-020-00028-z.